EGMSpy: an open-source Python toolkit for scalable data handling, classification, clustering, and visualisation of Copernicus EGMS InSAR data

A non-peer reviewed preprint submitted to EarthXiv

F. Catani*[1], C. Palmieri[1], R. Todde[1], L. Nava[2], and M. Floris[1]

[1]Department of Geosciences – MISSLab (Machine Intelligence and Slope Stability Lab),
University of Padova, Padova, Italy
[2]Institute for Artificial Intelligence, King's College, London, United Kingdom

April 2026

Abstract

The Copernicus European Ground Motion Service (EGMS) provides millimetre-accuracy line-of-sight displacement measurements for over five billion coherent scatterers across Europe, derived from Sentinel-1 SAR interferometry over the period 2015–2023. Despite the unprecedented spatial coverage and measurement density of this dataset, no open-source integrated toolchain exists for processing, classifying, clustering, and interactively visualising EGMS data at the regional to continental scale without resorting to subsampling or proprietary software. In this paper, we introduce **EGMSpy**, a fully open-source Python pipeline that ingests raw EGMS L2b CSV tiles, compresses them into a federated split-GeoParquet database (metadata and time series stored separately, linked by a unique point identifier), applies a physics-informed hybrid rule/GMM time series classifier to assign each point to a geophysical deformation class, groups spatially and dynamically coherent deforming areas using a velocity-weighted three-dimensional DBSCAN algorithm, and serves the entire dataset to an interactive Leaflet.js web viewer via a Flask/DuckDB REST bridge capable of sub-100 ms viewport queries over hundreds of millions of points. The pipeline is demonstrated on the northern Italy EGMS L2b dataset (2019–2023), comprising 434 tile pairs ($\approx$300 million coherent scatterers, 104 GB on disk), processed on a single workstation. Internal quality control confirms that the toolkit's OLS-derived velocity features are consistent with the official EGMS pre-computed velocities (RMSE $= 0.096\,\mathrm{mm\,yr^{-1}}$, bias $= -0.001\,\mathrm{mm\,yr^{-1}}$, $r = 0.9993$, $n = 99{,}751$). All code is released under the MIT licence and is available at `https://github.com/fcatani/EGMSpy` (repository in preparation).

---

*Corresponding author: filippo.catani@unipd.it

Keywords: InSAR; EGMS; GeoParquet; DuckDB; time series classification; DBSCAN; geohazard; subsidence

1 Introduction

1.1 The EGMS dataset and its challenges at scale

Satellite SAR interferometry (InSAR) is widely recognised as one of the primary tools for monitoring ground deformation at the regional scale, with millimetre-level accuracy in the detection of surface displacements associated with landslides, ground subsidence, volcanic activity, seismic deformation, and structural instability (Ferretti et al., 2001; Berardino et al., 2002; Hooper et al., 2012). The Copernicus *European Ground Motion Service* (EGMS; Crosetto et al. 2020; Costantini et al. 2017) represents the most ambitious application of InSAR to date, providing GNSS-calibrated line-of-sight (LOS) displacement time series for over five billion coherent scatterers across all Copernicus Participating States at an average spatial density of ≈ 1 point per $20\,\mathrm{m}^2$ in urban areas.

Despite its extraordinary coverage, the operational use of EGMS data presents several challenges. (i) A single national coverage may contain 10^8–10^9 points. The CSV format distributed by the portal is poorly suited to large-scale analytical queries; a single tile can exceed 2 GB. (ii) Different orbital tracks have different acquisition schedules, producing CSV files with different sets of date columns. Federating these into a single queryable database requires schema-aware handling. (iii) Each point's time series may exhibit linear trends, acceleration, seasonal signals, abrupt jumps, or noise-dominated behaviour. No automated, physics-informed classifier exists for the EGMS product. (iv) Identifying spatially coherent groups of deforming points (e.g. a landslide body, a subsiding building) requires clustering in a joint spatial–velocity space, not simple 2D spatial grouping. (v) The EGMS portal viewer is limited to pre-defined spatial extents and does not support classification-based colour coding or multi-point time series overlay. Standard GIS tools (QGIS, ArcGIS) struggle with tens of millions of points.

1.2 Existing tools and their limitations

Several open-source InSAR processing packages exist for generating displacement time series from raw SAR data: MintPy (Yunjun et al., 2019), StaMPS (Hooper, 2008), SNAP/STAMPS, and GAMMA (Werner et al., 2000). However, these tools operate *upstream* of the EGMS product — they produce displacement time series from raw Sentinel-1 SLC data, which requires significant computational resources and expertise.

For users who wish to *analyse* the already-processed EGMS product downstream, no equivalent open-source toolchain exists. The EGMS Explorer portal provides a web viewer and individual tile downloads, but offers no programmatic API, no time series classification, no clustering, and no ability to handle multi-tile datasets as a single queryable database. EGMStoolkit (Hrysiewicz et al., 2024) provides automated download functionality but does not address storage, classification, or visualisation.

1.3 Scope and contributions of this work

This paper presents **EGMSpy**, a Python pipeline that addresses the five challenges outlined above. The specific contributions are:

1. A **split-GeoParquet storage architecture** with DuckDB federation that reduces

CSV storage by ≈70% and enables sub-100 ms analytical queries over 1E08 points on a single workstation.

2. A **physics-informed hybrid time series classifier** assigning each EGMS point to one of seven geophysical classes (stable, noisy, linear, accelerating, decelerating, variable, other) plus four boolean descriptor flags (periodic, jumpy, variable, noisy_trend), using an 18-feature vectorised extraction pipeline followed by a rule-primary / GMM-secondary decision architecture.
3. A **velocity-weighted 3D DBSCAN clustering algorithm** that simultaneously enforces spatial proximity and velocity similarity, producing geophysically meaningful deformation clusters with convex-hull polygon outputs.
4. A **two-level sub-clustering** step that stratifies parent clusters by time series class, enabling differentiation of spatially co-located but behaviourally distinct deformation phenomena.
5. An **interactive web viewer** capable of rendering up to 200,000 filtered and classified InSAR points in a single Canvas 2D pass, with adaptive zoom-level spatial thinning, time series pop-up plots, and cluster polygon overlays.
6. A **PyQt6 GUI** orchestrating the full pipeline, making the toolkit accessible without command-line expertise.

2 Data

2.1 EGMS L2b product

The EGMS Level 2b product contains GNSS-calibrated LOS displacement time series derived from Sentinel-1 IW mode SAR data processed with the Persistent Scatterer InSAR (PSI) and Small Baseline Subset (SBAS) techniques. Each measurement point is characterised by 24 metadata attributes (Table 1) including mean LOS velocity, temporal coherence, orbital geometry, and LOS unit vector components, followed by $N_t \approx$ 200–300 displacement observations (mm) at dates spanning the 2015–2023 period (2019–2023 for the current release used here). Data are freely accessible via the Copernicus Land Monitoring Service portal (`https://egms.land.copernicus.eu/`) subject to the Copernicus Data Policy.

2.2 Demonstration area: Northern Italy

We demonstrate the EGMSpy pipeline on a test area that covers northern Italy, including the Po River Basin and surrounding pre-Alpine and Alpine foothills, bounded approximately by 6.55°E–14.02°E, 43.63°N–47.18°N (Fig. 2). This region is characterised by a wide variety of deformation phenomena: widespread agricultural and urban subsidence in the Po plain and delta (Colesanti et al., 2003; Raspini et al., 2019), active landsliding on Alpine and Apennine slopes (**?**), and seasonal signals associated with groundwater fluctuations and frost-heave, global warming-related processes in mountain areas.

The dataset comprises 433 tile pairs processed from 517 originally downloaded tiles (83 tiles were excluded due to zero valid measurements, typically covering sea or other low-backscatter areas). The total point count is approximately **300 million coherent scatterers** across 11 Sentinel-1 orbital tracks (ascending tracks 015, 022, 044, 066, 088, 095, 117, 139; descending tracks 146, 161, 168). The raw data occupy approximately 180 GB as EGMS ZIP archives; after conversion to split uncompressed GeoParquet the processed dataset occupies 104 GB (22.8 GB metadata, 81.6 GB time series).

3 Design and Implementation

3.1 Overview and pipeline architecture

The EGMSpy pipeline consists of nine sequential processing steps (Fig. 1), each implemented as an independent Python script callable from both the command line and the PyQt6 GUI. All processing steps are non-destructive: each step only *adds* columns to the metadata Parquet files; the time series Parquet files are never modified after the initial conversion and their information content remains consistent with the original EGMS product, unless data gaps are corrected.

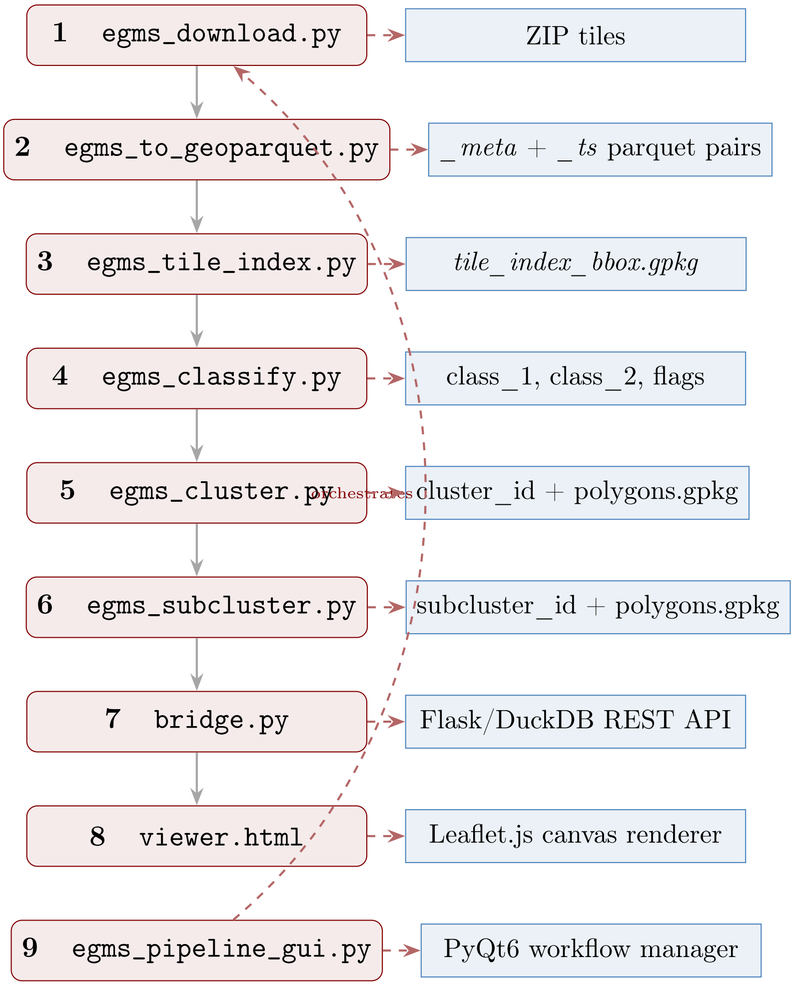

Figure 1: Full processing pipeline. Each step adds new columns to the `_meta.parquet` files (classification labels, cluster IDs) while the `_ts.parquet` files remain unchanged after conversion. The PyQt6 GUI (step 9) orchestrates all steps as monitored subprocesses.

3.2 Storage: split GeoParquet and DuckDB federation

Storage is one of the critical bottlenecks in big-data analysis, and InSAR is not an exception when the datasets cover regions or countries at a density such as the one provided by the EGMS service.

In EGMSpy, storage efficiency is increased by converting each input CSV tile into two coupled Parquet files: (i) the `<stem>_meta.parquet` file — where the 24 EGMS metadata columns plus derived columns (`orbit`, `max_gap_days`, `n_acquisitions`) and WGS84 `geometry` are stored in GeoParquet 1.0, EPSG:4326 format with Snappy compression; and (ii) the `<stem>_ts.parquet` file — where the time series with `pid` plus one float32 column per acquisition date (200–300 columns) is permanently memorised.

Files within a pair *meta/ts* are linked by the unique point identifier `pid`. All metadata files across all tiles are federated into a single DuckDB virtual view at query time:

```sql
CREATE VIEW all_metadata AS
  SELECT * FROM read_parquet(’processed/**/*_meta.parquet’,
                             union_by_name=True)
```

Table 1: EGMS L2b metadata columns (24 fixed) common to every tile.

#	Column	Description
1	`pid`	Unique point identifier (alphanumeric string)
2	`mp_type`	Measurement point type (0 = PS, 1 = DS)
3	`latitude`	WGS84 latitude (°, float64)
4	`longitude`	WGS84 longitude (°, float64)
5	`easting`	LAEA EPSG:3035 easting (m, float32)
6	`northing`	LAEA EPSG:3035 northing (m, float32)
7	`height`	Ellipsoidal height above LAEA datum (m)
8	`height_wgs84`	Ellipsoidal height above WGS84 ellipsoid (m)
9	`line`	SAR image line index (integer)
10	`pixel`	SAR image pixel index (integer)
11	`rmse`	Deformation model RMSE (mm)
12	`temporal_coherence`	Temporal coherence [0–1]
13	`amplitude_dispersion`	Amplitude dispersion index
14	`incidence_angle`	Satellite incidence angle (°)
15	`track_angle`	Satellite track heading angle (°)
16	`los_east`	LOS unit vector, east component
17	`los_north`	LOS unit vector, north component
18	`los_up`	LOS unit vector, vertical component
19	`mean_velocity`	Mean LOS velocity ($\mathrm{mm\,yr^{-1}}$)
20	`mean_velocity_std`	Mean velocity standard deviation ($\mathrm{mm\,yr^{-1}}$)
21	`acceleration`	LOS acceleration ($\mathrm{mm\,yr^{-2}}$)
22	`acceleration_std`	Acceleration standard deviation ($\mathrm{mm\,yr^{-2}}$)
23	`seasonality`	Seasonal amplitude (mm)
24	`seasonality_std`	Seasonal amplitude standard deviation (mm)

The `union_by_name=True` flag handles schema heterogeneity between orbital tracks (different acquisition date columns per track). Metadata columns are stored as float32 (except WGS84 coordinates retained at float64), achieving approximately 70% file size reduction relative to the original CSV. All spatial computations (DBSCAN, convex hulls) use EPSG:3035 (LAEA Europe) for equal-area distance preservation, while geometry storage and web display use EPSG:4326.

3.3 Spatial tile index

After conversion, a spatial QC index is built from all metadata files by `egms_tile_index.py` (Fig. 2).

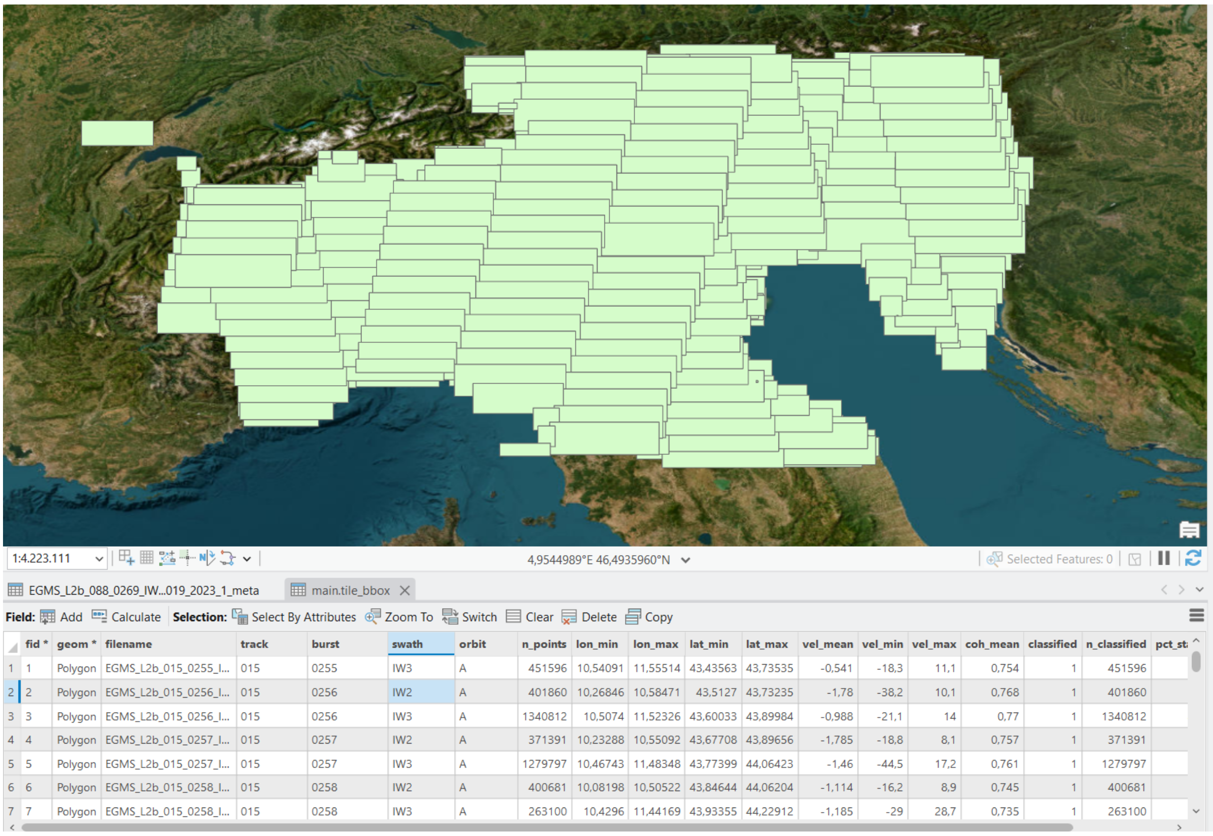

	fid *	geom *	filename	track	burst	swath	orbit	n_points	lon_min	lon_max	lat_min	lat_max	vel_mean	vel_min	vel_max	coh_mean	classified	n_classified	pct_st
1	1	Polygon	EGMS_L2b_015_0255_I...	015	0255	IW3	A	451596	10,54091	11,55514	43,43563	43,73535	-0,541	-18,3	11,1	0,754	1	451596	
2	2	Polygon	EGMS_L2b_015_0256_I...	015	0256	IW2	A	401860	10,26846	10,58471	43,5127	43,73235	-1,78	-38,2	10,1	0,768	1	401860	
3	3	Polygon	EGMS_L2b_015_0256_I...	015	0256	IW3	A	1340812	10,5074	11,52326	43,60033	43,89984	-0,988	-21,1	14	0,77	1	1340812	
4	4	Polygon	EGMS_L2b_015_0257_I...	015	0257	IW2	A	371391	10,23288	10,55092	43,67708	43,89656	-1,785	-18,8	8,1	0,757	1	371391	
5	5	Polygon	EGMS_L2b_015_0257_I...	015	0257	IW3	A	1279797	10,46743	11,48348	43,77399	44,06423	-1,46	-44,5	17,2	0,761	1	1279797	
6	6	Polygon	EGMS_L2b_015_0258_I...	015	0258	IW2	A	400681	10,08198	10,50522	43,84644	44,06204	-1,114	-16,2	8,9	0,745	1	400681	
7	7	Polygon	EGMS_L2b_015_0258_I...	015	0258	IW3	A	263100	10,4296	11,44169	43,93355	44,22912	-1,185	-29	28,7	0,735	1	263100	

Figure 2: Spatial tile index for the northern Italy demonstrator area, visualised in ArcGIS. Each polygon represents the bounding box of one EGMS L2b tile (434 valid tiles shown). The attribute table (lower panel) records, for each tile: track, burst, swath, orbit direction, point count (`n_points`), geographic extent, mean/min/max velocity, mean coherence, and classification status (`classified`, `n_classified`). Tiles covering open sea and high-Alpine terrain above the vegetation/infrastructure line contain few or no coherent scatterers and appear as sparse or empty tiles in the index. The full dataset covers approximately 6.5°E–14.0°E, 43.6°N–47.2°N, spanning the Po Plain, pre-Alpine foothills, Alpine chain, and northern Apennines.

For each tile, the script reads only the columns needed (`pid`, `longitude`, `latitude`, `mean_velocity`, `temporal_coherence`, `orbit`, `class_1` if present), computes the axis-aligned bounding box $[\lambda_{\min}, \phi_{\min}, \lambda_{\max}, \phi_{\max}]$, and reports classification coverage (% of rows with non-null `class_1`). In the demonstrator, processing is parallelised with `joblib` (threading backend); all 434 tiles are indexed in ≈5 min at 1.55 files s^{-1} using 16 workers. The output GeoPackage (`tile_index_bbox.gpkg`, EPSG:4326) is directly loadable in QGIS and enables immediate visual QC of coverage and classification completeness by styling on the `classified` attribute.

3.4 Winter-gap correction

SAR acquisitions over Alpine and high-elevation terrain are frequently suspended during winter months (predominantly November–March) due to snow cover causing temporal decorrelation and loss of coherent scatterers. These gaps produce stretches of null values in the `_ts.parquet` time series that, if left untreated, bias the OLS slope and harmonic fits in `egms_classify.py` by distorting the effective time baseline. The additional EGMSpy module `egms_correct.py` detects contiguous null runs exceeding a configurable minimum duration (default: 30 days) and fills them with gap-preserving linear interpolation between the last valid value before and the first valid value after each gap. The interpolated values are flagged and excluded from jump detection; the maximum gap duration (`max_gap_days`) is recorded as a derived metadata column and can be used as a data-quality filter in downstream queries. The quality check result in Section 4.1 confirms that this procedure introduces no detectable bias in the OLS velocity (residual bias = $-0.001\,\mathrm{mm\,yr^{-1}}$).

3.5 Time series classification

3.5.1 Overview and design strategy

At national and continental scales, InSAR ground deformation heuristic interpretation might be rendered impossible by the sheer amount of data available, if not supported by automation. Early approaches relied on hand-crafted statistical features combined with rule-based or supervised classifiers to distinguish stable, linear, and non-linear trend patterns (Berti et al., 2013; Cigna et al., 2011; Mirmazloumi et al., 2022). More recent work has moved toward deep learning architectures, including CNN–LSTM models that jointly exploit temporal deformation patterns and spatial morphological context to classify the entire deformation areas into geophysical process types such as landslides, subsidence, mining, or deep-seated gravitational deformations (Dong et al., 2025). However, process-level classification of spatially aggregated objects requires that individual measurement points have already been assigned kinematic labels — a per-point characterisation that existing frameworks do not provide at the scale of continental InSAR products such as EGMS. EGMSpy addresses this gap through a physics-informed hybrid rule/GMM classifier that assigns each of the ≈283 M northern Italy PS points to one of seven geophysical classes, operating directly on the per-point displacement time series without requiring spatial aggregation or auxiliary geomorphological data. Specifically, `egms_classify.py` implements a **hybrid rule-primary / GMM-secondary** classifier (v3 scheme). The key design principle is that physics-based rule labels are *final and cannot be overridden*: the Gaussian Mixture Model (GMM) is applied only to genuinely ambiguous residual points (those unresolved by all rules). This architecture prevents the minority-class collapse observed in pure GMM approaches, where classes such as *noisy* and *variable* are absorbed into the dominant *stable* class when GMM components are initialised without physics-based constraints.

3.5.2 Classification scheme

The classification of displacement time series into physically interpretable deformation categories is a prerequisite for operational geohazard analysis at all scales. Different surface processes — including ground subsidence, accelerating slope failures, seasonally driven creep, and abrupt infrastructure displacements — produce kinematically distinct time series signatures that, if left undifferentiated, cannot be exploited for early warning or risk mitigation (Casagli et al., 2023; Berti et al., 2013; Cigna et al., 2011). Translating raw velocity fields into labelled deformation classes (and clusters) enables the triage of hazard-relevant signals from the dominant background of stable or noise-dominated scatterers, directly supporting the prioritisation of field inspections and the calibration of physically based failure-forecasting models (Casagli et al., 2023; Mirmazloumi et al., 2022). Seven primary classes and four boolean descriptor flags are defined here, drawing on classification schemes proposed across multiple natural and anthropogenic hazard contexts — including slow-moving landslides, urban subsidence, mining deformation, and seasonal groundwater cycling (Berti et al., 2013; Cigna et al., 2011; Mirmazloumi et al., 2022; Dong et al., 2025) — so that the taxonomy covers the full kinematic diversity observable in a continental-scale product such as EGMS without imposing process-specific assumptions at the classification stage (Table 2).

Table 2: Time series classification scheme (v3). Primary classes are mutually exclusive; descriptor flags are independent and may co-occur with any primary class.

Code	**Class**	**Criterion**
0	stable	$\lvert v\rvert < v_s$, RMSE after linear detrend $\leq \sigma_n$
1	noisy	$\lvert v\rvert < v_s$, RMSE after linear detrend $> \sigma_n$
2	linear	$\lvert v\rvert \geq v_s$, sustained trend ($R^2_{\text{lin}} \geq 0.65$)
3	accel	Accelerating deformation (sign-consistent v_{diff} and quadratic improvement)
4	decel	Decelerating deformation
5	variable	$\lvert v\rvert < v_s$, erratic signal (high CUSUM, low R^2)
6	other	Ambiguous residual, resolved by GMM

Descriptor flag	**Criterion**
`periodic`	Seasonal harmonic significant: $R^2_{\text{seas}} - R^2_{\text{lin}} > 0.15$
`jumpy`	≥ 1 non-seasonal step $\geq j_{\text{min}}$ mm in deseasonalised residuals
`variable_flag`	High CUSUM changepoint score (erratic rate changes)
`noisy_trend`	Moving point ($\lvert v\rvert \geq v_s$) with high scatter after full detrend and deseasoning

3.5.3 Feature extraction

For each point, 18 scalar features are extracted from the LOS displacement time series $\{d_1, \ldots, d_{N_t}\}$ (mm) at times $\{t_1, \ldots, t_{N_t}\}$ (fractional years). The feature set draws on parameterisations established in the InSAR time series classification literature (Berti et al., 2013; Cigna et al., 2011; Mirmazloumi et al., 2022), extended here with a harmonic decomposition (Chen et al., 2026) and a CUSUM-based changepoint score (Ghaderpour et al., 2024) to capture seasonal signals and rate instability respectively. All computations are vectorised over the full $M \times N_t$ chunk array using batch NumPy Ordinary Least Squares via `einsum`, avoiding any Python loop over points (Table 3). The choice of OLS unweighted estimator over a more rigorous one such as Theil-Shen, is justified by the computational constraint of processing 10^8–10^9 points, and by the demonstrated consistency of OLS estimations with the official EGMS velocities (see 4.1).

Linear model. The design matrix for a centred linear fit is:

$$\mathbf{L} = \begin{pmatrix} 1 & t_1 - \bar{t} \\ \vdots & \vdots \\ 1 & t_{N_t} - \bar{t} \end{pmatrix} \tag{1}$$

The OLS solution $\hat{\boldsymbol{\beta}} = (\mathbf{L}^\top \mathbf{L})^{-1} \mathbf{L}^\top \mathbf{d}$ yields the mean velocity $v = \hat{\beta}_1$ (mm yr^{-1}) and the coefficient of determination:

$$R^2_{\text{lin}} = 1 - \frac{\|\mathbf{d} - \mathbf{L}\hat{\boldsymbol{\beta}}\|^2}{\|\mathbf{d} - \bar{d}\|^2} \tag{2}$$

Split-half velocities. Separate OLS slopes are fitted to the first and second halves of the time span ($I_1 = \{i : i < N_t/2\}$, $I_2 = \{i : i \geq N_t/2\}$), giving v_1 and v_2. Their difference:

$$v_{\text{diff}} = v_2 - v_1 \quad (\text{mm}\,\text{yr}^{-1}) \tag{3}$$

is the primary indicator of acceleration or deceleration.

Harmonic (seasonal) fit. Annual and semi-annual harmonics are fitted jointly with the linear trend:

$$\mathbf{H} = \begin{pmatrix} 1 & \tau_1 & \cos 2\pi t_1 & \sin 2\pi t_1 & \cos 4\pi t_1 & \sin 4\pi t_1 \\ \vdots & \vdots & \vdots & \vdots & \vdots & \vdots \end{pmatrix} \tag{4}$$

where $\tau = t - \bar{t}$. The `periodic` flag is set when the R^2 improvement over the linear-only fit exceeds 0.15.

Quadratic fit. The quadratic coefficient $\hat{\gamma}_2$ (mm yr^{-2}) from fitting $\mathbf{Q} = [1, \tau, \tau^2]$ quantifies the rate of velocity change. Its R^2 improvement over the linear fit, q_{R^2}, is used jointly with v_{diff} to detect acceleration and deceleration.

Jump detection. First differences of the deseasonalised residuals $r_i = d_i - \hat{d}_i^{(\text{harm})}$ are examined for abrupt steps:

$$\delta_i = r_i - r_{i-1} \tag{5}$$

The `jumpy` flag is set when ≥ 1 step satisfies $|\delta_i| \geq j_{\min}$ outside the seasonal envelope.

CUSUM changepoint score.

$$S_k = \sum_{i=1}^{k} (r_i - \bar{r}), \qquad \text{cusum\_score} = \frac{\max_k S_k - \min_k S_k}{\sigma_r \sqrt{N_t}} \tag{6}$$

A high CUSUM score indicates an erratic or non-stationary deformation signal and drives the `variable_flag`.

Table 3: Complete 18-feature vector extracted per InSAR point.

Idx	Name	Description
0	`v_robust`	OLS slope: mean LOS velocity ($\mathrm{mm\,yr^{-1}}$)
1	`v_first_half`	Mean velocity, first 50% of time span
2	`v_second_half`	Mean velocity, second 50% of time span
3	`v_diff`	$v_2 - v_1$ ($\mathrm{mm\,yr^{-1}}$)
4	`rmse_detrended`	RMSE after linear detrend (mm)
5	`rmse_deseason`	RMSE after detrend + harmonic removal (mm)
6	`seasonal_amp`	Annual harmonic amplitude (mm)
7	`seasonal_r2`	R^2 of harmonic fit on detrended series
8	`quad_coeff`	Quadratic coefficient ($\mathrm{mm\,yr^{-2}}$)
9	`quad_r2`	R^2 improvement: quadratic over linear
10	`n_jumps_nonseas`	Count of non-seasonal steps $\geq j_{\min}$
11	`jump_max_mm`	Largest step magnitude (mm)
12	`n_valid_frac`	Fraction of non-null acquisitions
13	`acf_lag1`	Lag-1 autocorrelation of detrended residuals
14	`cusum_score`	CUSUM changepoint score (normalised)
15	`velocity_r2`	R^2 of linear fit
16	`range_mm`	Total range $\max(d) - \min(d)$ (mm)
17	`noise_p90`	90th percentile of $\lvert\delta_i\rvert$

3.5.4 Rule-based classification

Rules are evaluated in strict priority order on the standardised feature vector of each point; the first matching condition assigns the final label and evaluation halts. Default parameters for the North Italy demonstrator dataset are: $v_s = 2.5\,\mathrm{mm\,yr^{-1}}$, $\sigma_n = 3.0\,\mathrm{mm}$, $\theta_q = 0.15$, $c_{\text{thresh}} = 1.5$.

Algorithm 1 Rule-primary classifier (applied independently per point)

```
Require: feature vector ($v$, rmse_dt, cusum, $R^2_{\text{lin}}$, $q_{R^2}$, $v_{\text{diff}}$, $\hat{\gamma}_2$); thresholds $v_s$, $\sigma_n$, $\theta_q$, $c_{\text{thresh}}$
Ensure: class label $\ell \in \{0, 1, 2, 3, 4, 5, 6\}$
if $|v| < v_s$ then
    if rmse_dt $\leq \sigma_n$ then
        return $\ell = 0$    (stable)
    else if cusum $> c_{\text{thresh}}$ and $R^2_{\text{lin}} < 0.5$ then
        return $\ell = 5$    (variable)
    else
        return $\ell = 1$    (noisy)
    end if
else                                                    ▷ $|v| \geq v_s$: moving point
    if $q_{R^2} > \theta_q$ and $R^2_{\text{lin}} < 0.85$ then
        if $\text{sgn}(v_{\text{diff}}) = \text{sgn}(v)$ and $\hat{\gamma}_2 \cdot v < 0$ then
            return $\ell = 3$    (accel)
        else if $\text{sgn}(v_{\text{diff}}) \neq \text{sgn}(v)$ and $\hat{\gamma}_2 \cdot v > 0$ then
            return $\ell = 4$    (decel)
        end if
    end if
    if $R^2_{\text{lin}} \geq 0.65$ then
        return $\ell = 2$    (linear)
    end if
    return $\ell = 6$    (other — deferred to GMM)
end if
```

3.5.5 GMM secondary classification

Points unresolved by rules (label $= -1$) are passed to a Gaussian Mixture Model fitted on the standardised 18-feature space. GMM component means are seeded from the centroids of rule-labelled points:

$$\boldsymbol{\mu}_k^{(0)} = \frac{1}{|C_k|} \sum_{i \in C_k} \mathbf{x}_i \tag{7}$$

where C_k denotes the set of rule-classified points for class k. The number of components is $K = 5$. Rule-assigned labels are never replaced; the GMM resolves only the `other` residual class. Classification outputs written back to `_meta.parquet` are: `class_1`, `class_2`, `class_prob_1` (1.0 for rule-assigned; GMM posterior probability for `other`), and the four boolean descriptor flags.

3.6 Velocity-weighted 3D DBSCAN clustering

3.6.1 Motivation

Standard 2D spatial clustering (including Euclidean DBSCAN) groups spatially proximate points regardless of their deformation rate. As an example, a cluster spanning both $-15\,\text{mm}\,\text{yr}^{-1}$ subsiding points and $+2\,\text{mm}\,\text{yr}^{-1}$ stable points has no geophysical meaning.

The 3D approach described here ensures that two points are density-connected only when they are simultaneously spatially proximate and dynamically similar.

3.6.2 3D feature space and velocity rescaling

The velocity axis is rescaled so that a velocity difference of $\varepsilon_v\,\mathrm{mm\,yr^{-1}}$ is geometrically equivalent to ε_m m of spatial separation:

$$w_v = \frac{\varepsilon_m}{\varepsilon_v} \tag{8}$$

The 3D input to DBSCAN becomes, therefore:

$$\mathbf{x}_i = \begin{pmatrix} E_i \\ N_i \\ v_i \cdot w_v \end{pmatrix} \in \mathbb{R}^3 \tag{9}$$

where E_i, N_i are LAEA easting/northing (m) and v_i is mean LOS velocity ($\mathrm{mm\,yr^{-1}}$). The single DBSCAN radius $\varepsilon = \varepsilon_m$ then simultaneously enforces:

$$\sqrt{(E_i - E_j)^2 + (N_i - N_j)^2 + (v_i - v_j)^2 w_v^2} \;\le\; \varepsilon_m \tag{10}$$

which is approximately equivalent to requiring both $\sqrt{(E_i - E_j)^2 + (N_i - N_j)^2} \le \varepsilon_m$ and $|v_i - v_j| \le \varepsilon_v$.

3.6.3 Algorithm and cluster characterisation

Only eligible points are passed to DBSCAN, which satisfy the condition: $|v| \ge v_{\min}$ and $\gamma \ge \gamma_{\min}$ ($v_{\min} = 2.5\,\mathrm{mm\,yr^{-1}}$, $\gamma_{\min} = 0.5$ for the demonstrator case). DBSCAN (Ester et al., 1996) is run with `eps=` ε_m, `algorithm=ball_tree`, `n_jobs=-1` (all cores). For each resulting cluster, class purity $\rho = n_{\text{dominant}}/n_{\text{total}}$ is computed; clusters below $\rho_{\min} = 0.5$ are flagged as mixed. Cluster polygons are computed as convex hulls (via `scipy.spatial.ConvexHull`) buffered by $b_m = 20$ m with rounded cap and join styles (`resolution=32`), reprojected to EPSG:4326 for output. Cluster IDs follow the format `CL_nnnn`. Buffering with rounded caps is used to preserve geomorphological consistency and is based on the local approximate Sentinel-1 pixel resolution.

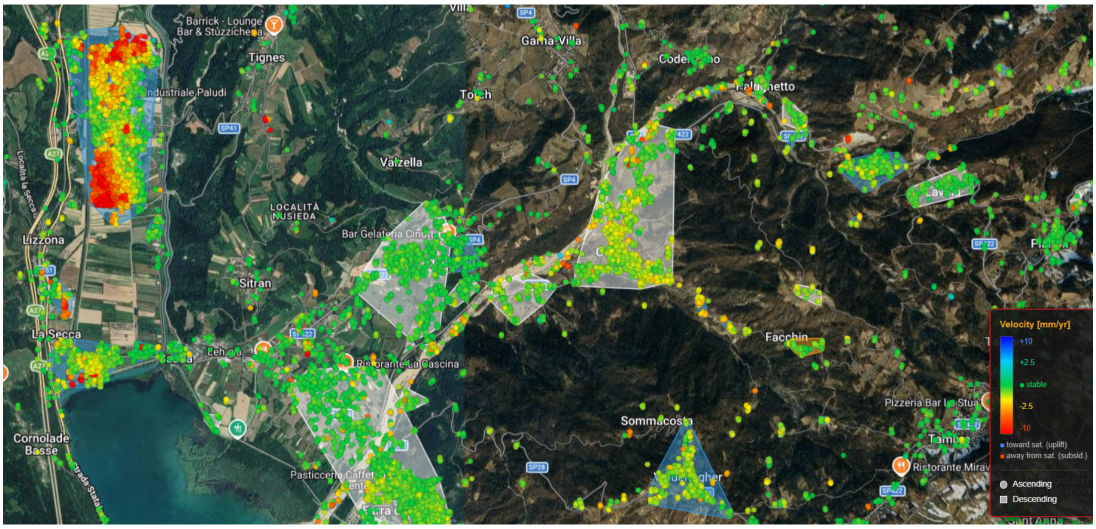

Figure 3: Example output of the velocity-weighted 3D DBSCAN clustering step for a peri-Alpine area in the Belluno province (Veneto, NE Italy). Coloured circles and squares represent InSAR measurement points coloured by mean LOS velocity (red = away from satellite, blue = towards satellite, green = stable) using the official EGMS colour scale. Ascending-orbit points are shown as circles and descending-orbit points as squares. Semi-transparent grey polygons are cluster convex hulls buffered by 20 m, each grouping spatially proximate points within $\varepsilon_m = 100\,\mathrm{m}$ and $\varepsilon_v = 3\,\mathrm{mm\,yr^{-1}}$. The red/orange cluster (upper left) corresponds to an industrial area undergoing active subsidence; the smaller clusters across the scene highlight individual buildings, road embankments and hillslope sectors with coherent deformation signals.

3.7 Per-class sub-clustering

3.7.1 Motivation

First-order (or parent) clusters may span large areas and contain spatially distinct deformation sub-patterns that share similar average velocities but differ in temporal behaviour or in the kinematics. Sub-clustering stratifies each parent cluster by TS class and runs a secondary DBSCAN within each stratum (Fig. 4), producing group IDs of the form `CL_nnnn_SUB_mmm`. Embedding the parent cluster ID in the sub-cluster ID enables efficient DuckDB lookups without a join (`WHERE subcluster_id LIKE 'CL_0042%'`). Sub-clustering may support expert interpretation of deformations measured by InSAR and help in the correct identification of impending hazards. In case of large slope instabilities, such as deep-seated gravitational slope deformations, sub-clustering may also be fundamental for numerical model design and calibration.

3.7.2 Implementation

Eligible points are grouped on the compound key `cluster_id` + `class_1` using `pandas.groupby`; per-group DBSCAN tasks are dispatched sequentially, with sub-cluster IDs and convex-hull polygons accumulated and written back to the `_meta.parquet` files on completion. Per-group DBSCAN tasks are dispatched as a `joblib` generator with `return_as="generator"`, allowing write-back to begin while remaining groups are still computing. Sub-cluster IDs and polygon GeoPackage (`subclusters_polygons.gpkg`, EPSG:3035) are produced as outputs.

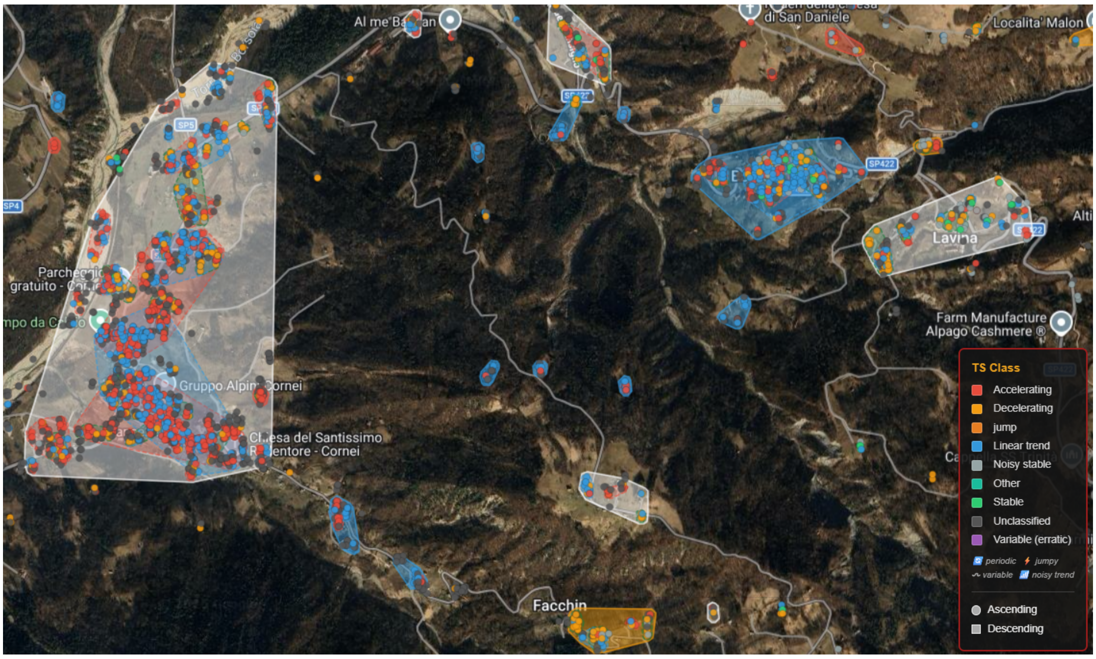

Figure 4: Sub-clustering output for the same peri-Alpine area shown in Fig. 3, with points coloured by time series classification class (red = accelerating, orange = decelerating, blue = linear trend, grey = noisy–stable, green = stable, purple = variable, olive = other). Sub-cluster polygons (semi-transparent fills in matching colours) delineate spatially and behaviourally coherent groups within each parent cluster. The mixture of accelerating (red) and linear (blue) points visible within the large left-hand cluster indicates spatially co-located areas with distinct deformation dynamics, separable only after TS classification. The legend (lower right) also shows the four descriptor flags (*periodic*, *jumpy*, *variable*, *noisy trend*) which are rendered as small icon overlays in the viewer.

3.8 DuckDB query layer and web visualisation

3.8.1 Flask/DuckDB bridge

The visualisation of data, classifications, and clusters is implemented with the combination of a query system fed by an interactive HTML viewer and a DuckDB database. The module `bridge.py` is a lightweight Flask server that exposes the DuckDB federated database to the browser via a REST API (Table 4). All queries run in-memory on a single persistent `duckdb.connect(":memory:")` instance. The viewport query uses a single Common Table Expression that computes both the spatially-thinned point set and the raw count in one execution plan, eliminating the concurrent-connection conflicts that arise from sequential queries when browser requests are aborted mid-flight:

```
WITH filtered AS (
    SELECT * FROM all_metadata
    WHERE latitude  BETWEEN :min_lat AND :max_lat
      AND longitude BETWEEN :min_lon AND :max_lon
```

```
      AND ABS(mean_velocity) >= :thresh
      AND temporal_coherence >= :min_coh ),
total_cte  AS ( SELECT COUNT(*) AS n FROM filtered ),
ranked     AS ( SELECT *,
    ROW_NUMBER() OVER (
        PARTITION BY FLOOR(latitude/:cell), FLOOR(longitude/:cell)
        ORDER BY temporal_coherence DESC ) AS _rn
    FROM filtered ),
thinned    AS ( SELECT * FROM ranked WHERE _rn=1 LIMIT :max_pts )
SELECT t.*, tc.n FROM thinned t CROSS JOIN total_cte tc
```

Table 4: REST API endpoints exposed by `bridge.py`.

Endpoint	Description
`GET /get_points`	Viewport + filter query with adaptive spatial thinning. Returns JSON array; headers `X-Total-Count`, `X-Rendered-Count`.
`GET /get_timeseries`	Full TS for one `pid`. Returns dates, values, gap annotations.
`GET /get_info`	DB statistics and feature flags (`has_classes`, `has_clusters`, etc.).
`GET /get_clusters`	Parent cluster polygons as GeoJSON.
`GET /get_subclusters`	Sub-cluster polygons as GeoJSON.
`GET /health`	Liveness check; used by GUI bridge monitor.

The spatial thinning grid cell size is zoom-adaptive (Table 5), ensuring that at low zoom levels only the highest-coherence representative per ≈13 km cell is returned, while at zoom ≥12 the cell size is smaller than the typical PS spacing and all points are returned.

Table 5: Adaptive spatial grid thinning parameters by Leaflet zoom level. At each cell, the point with highest temporal coherence is selected.

Zoom	Cell size (°)	Approximate ground size
5	0.120	≈13 km
8	0.015	≈1.5 km
10	0.004	≈400 m
12	0.001	≈100 m
≥12	0.001	All points (cell < PS spacing)

3.8.2 Canvas-based web viewer

`viewer.html` is a single self-contained file embedding Leaflet.js and a custom `EgmsCanvasLayer` renderer (Fig. 5). All points are drawn in a single `requestAnimationFrame` Canvas 2D pass with zero per-point DOM objects or event listeners. During pan, the canvas is shifted via CSS `transform` with no redraw; full redraw occurs only on `moveend` and `zoomend`. Hit testing uses a 32-pixel spatial grid index (O(1) per click). The hard cap of 200,000 rendered points is handled smoothly by the canvas renderer, compared to ≈10,000 for individual Leaflet markers.

Ascending-orbit points are rendered as circles and descending-orbit points as squares. Points are coloured by the official EGMS velocity scale (blue = uplift, green = stable, yellow/red = subsidence) or, optionally, by time series class. Ctrl+clicking multiple points opens overlapping time series in a floating panel with up to ten distinguishable colours.

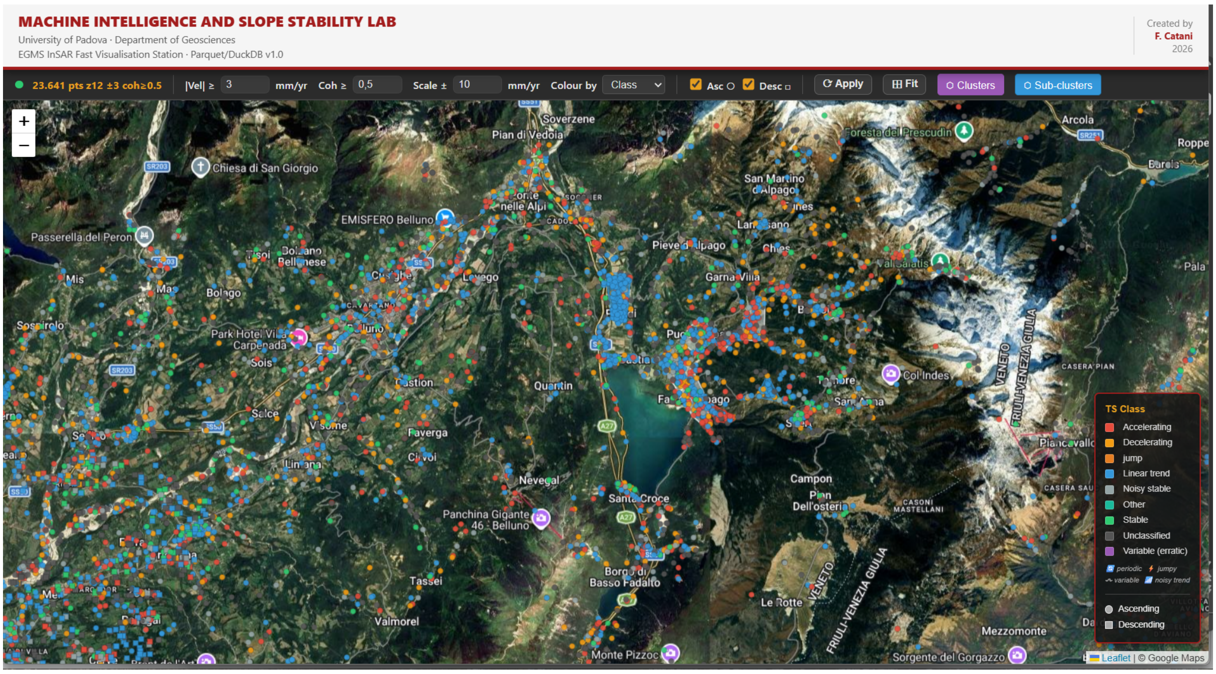
MACHINE INTELLIGENCE AND SLOPE STABILITY LAB
University of Padova · Department of Geosciences
EGMS InSAR Fast Visualisation Station · Parquet/DuckDB v1.0

Created by
F. Catani
2026

● 23.641 pts z12 ±3 coh≥0.5 |Vel| ≥ 3 mm/yr Coh ≥ 0,5 Scale ± 10 mm/yr Colour by Class ☑ Asc ○ ☑ Desc □

Figure 5: The MISSlab EGMS web viewer showing a portion of the Belluno–Alpago area (NE Italy, Veneto/Friuli-Venezia Giulia border). Points are coloured by time series class (legend, lower right); ascending-orbit points (Sentinel-1 tracks 015–139) are shown as circles and descending-orbit points (tracks 146–168) as squares. The viewer is displaying 23,641 points at zoom level 12 with $|v| \geq 3\,\mathrm{mm\,yr^{-1}}$ and coherence ≥ 0.5 filters applied; the status bar (top left) shows the current filter state. The toolbar provides controls for velocity/class colour mode, coherence threshold, velocity scale, orbit selection, and cluster/sub-cluster polygon overlay. The viewer supports sub-100 ms viewport queries over the full ≈300 M-point northern Italy database via the DuckDB/Flask bridge, enabling real-time interactive exploration comparable to a desktop GIS but without data subsampling.

4 Results

4.1 Pipeline quality control: velocity consistency

As an internal consistency check, we compared the EGMS pre-computed mean LOS velocity (`mean_velocity`, derived from the official EGMS weighted least-squares processing chain) against the OLS velocity independently recomputed by EGMSpy from the stored float32 time series. A random sample of 99,751 points was drawn from all 434 tile pairs and the two estimates compared (Fig. 6).

The two velocity estimates agree to within RMSE = $0.096\,\mathrm{mm\,yr^{-1}}$, bias = $-0.001\,\mathrm{mm\,yr^{-1}}$, Pearson $r = 0.9993$. Zero points in the sample deviated by more than $1\,\mathrm{mm\,yr^{-1}}$. The residual distribution is symmetric, centred at zero, and narrow — consistent with float32 quantisation noise (± 0.06 mm per value, propagating to $\approx 0.1\,\mathrm{mm\,yr^{-1}}$ in the OLS slope depending on time span). Panel (c) of Fig. 6 shows a horizontal residual band across the full velocity range $[-10, +10]\,\mathrm{mm\,yr^{-1}}$, confirming the absence of velocity-dependent systematic bias that would indicate errors in the winter-gap interpolation or the float32 conversion. The RMSE of $0.096\,\mathrm{mm\,yr^{-1}}$ is one order of magnitude below the EGMS L2b measurement precision ($\approx$0.5–1.0 $\mathrm{mm\,yr^{-1}}$; Crosetto et al. 2020).

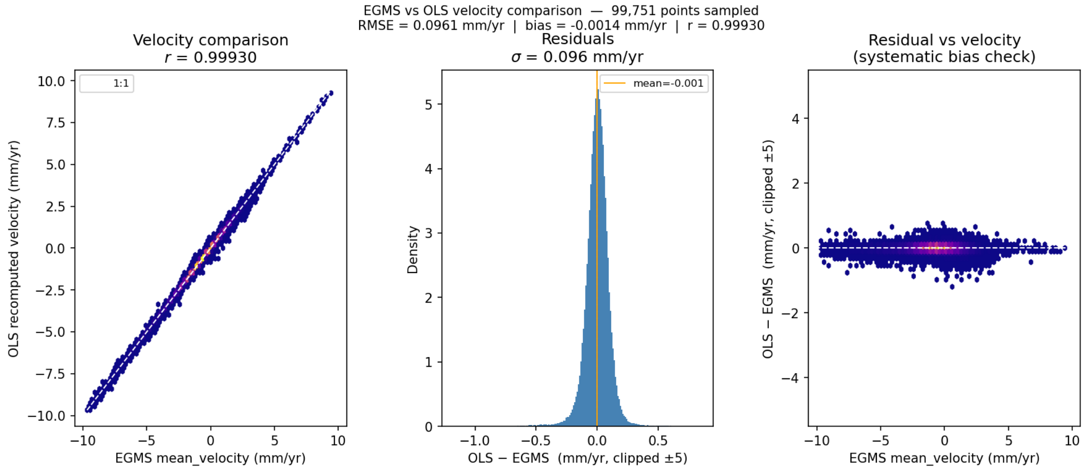

Figure 6: Internal quality check: comparison between the EGMS pre-computed mean LOS velocity and the OLS velocity recomputed by EGMSpy from the stored float32 time series, for a random sample of 99,751 points across all 434 northern Italy tiles (Copernicus EGMS L2b, 2019–2023). **(a)** Hexbin scatter (yellow = maximum density) showing near-perfect 1:1 agreement ($r = 0.9993$). **(b)** Residual distribution $\Delta v = v_{\mathrm{OLS}} - v_{\mathrm{EGMS}}$ ($\sigma = 0.096\,\mathrm{mm\,yr^{-1}}$, bias $= -0.001\,\mathrm{mm\,yr^{-1}}$); the sharp symmetric peak is characteristic of float32 quantisation noise. **(c)** Residuals vs. EGMS velocity, confirming no velocity-dependent bias across the full range. The RMSE is an order of magnitude below EGMS measurement precision ($\approx$0.5–1.0 $\mathrm{mm\,yr^{-1}}$; Crosetto et al. 2020), validating the toolkit's internal feature extraction and confirming that the winter-gap correction introduces no detectable velocity artefact.

4.2 Classification and clustering results

4.2.1 Demonstrator dataset overview

The northern Italy EGMS L2b database (2019–2023) processed with EGMSpy comprises **282,606,853 coherent scatterers** across 433 tile pairs, distributed nearly equally between ascending (137,713,488 points; 48.7%) and descending (144,893,365; 51.3%) Sentinel-1 geometries. The mean temporal coherence is $\bar{\gamma} = 0.756$ (median $= 0.77$), reflecting the predominantly urban and agricultural character of the Po Plain and pre-Alpine foothills where coherence is maintained across the full 2019–2023 observation period.

The overall velocity distribution is negatively skewed (mean $= -0.93\,\mathrm{mm\,yr^{-1}}$, median $= -0.8\,\mathrm{mm\,yr^{-1}}$, $\sigma = 1.98\,\mathrm{mm\,yr^{-1}}$), with a markedly asymmetric tail: the 5th percentile ($-3.5\,\mathrm{mm\,yr^{-1}}$) lies 3.2× further from zero than the 95th percentile ($+1.1\,\mathrm{mm\,yr^{-1}}$). This negative bias is a robust signal of widespread, low-rate subsidence across the study area, consistent with the well-documented Po Plain groundwater-driven consolidation (Colesanti et al., 2003; Raspini et al., 2019; Chen et al., 2026) and with the general tendency for InSAR LOS velocities in this region. Extreme velocities reach -101.5 and $+98.4\,\mathrm{mm\,yr^{-1}}$, with 1,588,542 points (0.56%) exceeding $|v| \geq 10\,\mathrm{mm\,yr^{-1}}$, indicative of localised rapid deformation such as active landslides, mining subsidence, and infrastructure settlement.

4.2.2 Time series classification

Of the 282,606,853 processed points, 276,281,109 (97.8%) were assigned a primary class label by the EGMSpy classifier; the remaining 2.2% remain unclassified, predominantly in Alpine areas with short valid time series ($n_{\text{valid}} < 10$ acquisitions) or extreme velocity outliers that fell outside all rule boundaries. Table 6 summarises the full class distribution.

Table 6: Time series classification results for the northern Italy EGMS L2b dataset (282,606,853 points, 434 tiles). Percentages refer to the total point count. Velocity statistics are given for each class.

Class	**N**	**%**	$\bar{v}$	σ_v	v_{P05}	v_{P95}
				$(\mathrm{mm\,yr^{-1}})$		
noisy–stable	148,002,066	52.4	−0.53	1.07	−2.2	+1.3
stable	103,877,470	36.8	−0.77	0.90	−2.2	+0.7
linear	16,293,143	5.8	−4.80	3.53	−10.9	−2.5
accel	4,473,766	1.6	−2.75	1.92	−4.7	+2.8
decel	3,634,636	1.3	−2.67	2.00	−4.7	+2.9
unclassified	6,325,744	2.2	−0.60	7.14	−7.5	+2.9
Total	**282,606,853**	**100**				

Stable and noisy–stable classes. The dominant classes are *noisy–stable* (52.4%) and *stable* (36.8%), together accounting for 89.2% of all points. Both classes are confined by definition to $|v| < v_s = 2.5\,\mathrm{mm\,yr^{-1}}$, and their velocity distributions are broadly similar (mean -0.53 and $-0.77\,\mathrm{mm\,yr^{-1}}$ respectively). The distinction between them is the residual scatter after linear detrending: *stable* points have low scatter (`rmse_dt` $\leq 3.0\,\mathrm{mm}$), while *noisy–stable* points exceed this threshold. The high proportion of *noisy–stable* points reflects the abundance of partly-coherent scatterers in agricultural and vegetated areas at the margins of the stable PS network, where temporal decorrelation introduces scatter without a systematic trend.

Unstable classes. Points classified as *linear*, *accel*, or *decel* together comprise 24,401,545 points (8.8% of classified points; Table 6). The *linear* class (n = 16,293,143; 5.8%) has a strongly negative mean velocity ($-4.80\,\mathrm{mm\,yr^{-1}}$, P50 = $-4.1\,\mathrm{mm\,yr^{-1}}$) with a negative-only 95th-percentile range ($v_{\text{P95}} = -2.5\,\mathrm{mm\,yr^{-1}}$), confirming that the vast majority of linearly-trending points represent steady subsidence. The *accel* class (n = 4,473,766; 1.6%) and *decel* class (n = 3,634,636; 1.3%) show similar velocity distributions (mean $\approx -2.7\,\mathrm{mm\,yr^{-1}}$), with the slight excess of accelerating over decelerating points (ratio 1.23:1) consistent with an ongoing consolidation trend that began before the observation window and has not yet reached equilibrium in many locations. Both classes exhibit wide 95th-percentile ranges that span into positive velocities, indicating that non-subsidence phenomena (slope failures, localised uplift, frost heave, permafrost degradation, infrastructure rebound) also contribute to these classes.

Descriptor flags. Table 7 summarises the four boolean descriptor flags, which are independent of and combinable with the primary class.

Table 7: Descriptor flag statistics. Flags are assigned independently of primary class and may co-occur with each other and with any primary class. Percentages refer to the total 282,606,853 classified points and sum to more than 100% because multiple flags may be set simultaneously on a single point.

Flag	**N**	**%**	**Interpretation**
`jumpy`	178,877,339	63.3	$\geq$1 abrupt step $\geq$ 5 mm
`variable_flag`	86,707,933	30.7	High CUSUM changepoint score
`periodic`	66,842,068	23.7	Significant annual/semi-annual harmonic
`noisy_trend`	9,983,537	3.5	Moving point with high residual scatter

The `jumpy` flag (63.3%) deserves careful interpretation: given that the *noisy–stable* class constitutes 52.4% of all points, and noisy time series intrinsically contain large first differences that may exceed the fixed 5 mm jump threshold, a substantial fraction of the `jumpy` flags in the noisy class represent measurement scatter rather than true geophysical step events. True geophysical jumps are more reliably identified when the `jumpy` flag co-occurs with *linear*, *accel*, or *decel* classes. The `periodic` flag (23.7%) indicates that nearly one in four coherent scatterers in northern Italy show a statistically significant annual or semi-annual harmonic component in its displacement time series, reflecting the region's strong seasonal groundwater fluctuations, agricultural irrigation cycles, and frost-heave signals in the peri-Alpine zone. The `variable_flag` (30.7%) captures points with erratic rate changes — a population that includes both geophysically meaningful episodic deformation (e.g. triggered landslide acceleration) and measurement artefacts from atmospheric phase screen residuals (Zebker et al., 1997), i.e. spatially-correlated tropospheric delay errors not fully removed during InSAR processing.

4.2.3 Spatial patterns of deformation across geomorphological zones

The dataset is partitioned into three elevation-based physiographic zones following the standard Italian geomorphological classification (Fredi and Lupia Palmieri, 2004): the plain and low-hill zone (point elevation < 600 m a.s.l., comprising the Po Plain, the Venetian lowland, and the Ligurian and Apennine foothills), the mid-mountain zone (600–1500 m), and the high-mountain zone (> 1500 m, corresponding to the Alpine chain proper and high Apennine crests). Table 8 reports the class distribution and velocity statistics per zone; the three zones reveal markedly different deformation regimes consistent with the known geomorphology of northern Italy.

Table 8: Class distribution and velocity statistics by physiographic zone. Zone boundaries follow the standard Italian geomorphological classification (Fredi and Lupia Palmieri, 2004): plain and low hill (<600 m a.s.l.), mid-mountain (600–1500 m), high mountain (>1500 m). Only classes with >0.1% zonal frequency are listed. $\bar{v}$ and σ_v in mm yr^{-1}.

Zone	Class	N	$\%_{\text{zone}}$	$\bar{v}$	σ_v	v_{P05}	v_{P95}
Plain / low hill	noisy	107,145,817	46.6	−0.75	1.01	−2.3	+1.0
	stable	97,846,072	42.6	−0.80	0.88	−2.2	+0.7
	linear	14,976,656	6.5	−4.81	2.92	−10.6	−2.6
	accel	4,034,150	1.8	−2.90	1.69	−4.7	+2.6
	decel	3,199,778	1.4	−2.84	1.72	−4.6	+2.6
Mid-mountain	noisy	16,386,357	68.9	−0.23	1.06	−2.0	+1.5
	stable	4,881,279	20.5	−0.35	1.05	−2.0	+1.3
	linear	782,216	3.3	−4.12	5.55	−12.3	+5.4
	accel	265,163	1.1	−1.79	2.77	−4.5	+3.5
	decel	275,040	1.2	−1.75	3.05	−5.0	+3.8
High mountain	noisy	24,469,892	83.9	+0.24	0.94	−1.3	+1.7
	stable	1,150,119	3.9	+0.12	1.48	−3.2	+2.5
	linear	534,271	1.8	−5.45	9.66	−21.3	+6.2
	accel	174,453	0.6	−0.58	3.23	−4.6	+3.4
	decel	159,818	0.5	−0.91	3.20	−4.7	+3.4

Plain and low-hill zone (<600 m a.s.l.; 229,682,099 points, 81.3% of total). This zone dominates the dataset by point count, reflecting the high PS density in urban and agricultural areas of the Po Plain and Po delta lowland where temporal coherence is well maintained over the full 2019–2023 observation window. The *linear* class reaches its highest zonal proportion here (6.5%), with a strongly negative velocity distribution ($\bar{v} = -4.81$ mm yr^{-1}; P95 $= -2.6$ mm yr^{-1}) — the entire upper 5th percentile of the distribution remains in land affected by subsidence. This pattern reflects the well-documented ongoing consolidation of Holocene alluvial deposits throughout the Po Plain (Colesanti et al., 2003; Teatini et al., 2005; Raspini et al., 2019), amplified by groundwater overexploitation in agricultural and urban areas. The *accel* class (1.8%) has a mean velocity of -2.90 mm yr^{-1}, indicating that accelerating deformation in this zone is predominantly confined to the subsidence domain, consistent with progressive alluvial deposits consolidation rather than gravity-driven kinematics. The overall velocity bias in this zone is the strongest of the three ($\bar{v}_{\text{noisy}} = -0.75$ mm yr^{-1}, $\bar{v}_{\text{stable}} = -0.80$ mm yr^{-1}), confirming that even nominally stable scatterers show a measurable systematic downward motion relative to the GNSS reference frame.

Mid-mountain zone (600–1500 m a.s.l.; 23,770,476 points, 8.4% of total). The mid-mountain zone is characterised by a strong shift toward noise-dominated signals: the *noisy–stable* class reaches 68.9%, substantially higher than in the plain but lower than in the high-mountain zone, reflecting the intermediate InSAR conditions of peri-Alpine valleys, Apennine ridges, and lower Alpine slopes where partial vegetation cover and seasonal snow reduce but do not eliminate coherence. The *linear* proportion (3.3%) is lower than in the plain, and its velocity distribution is markedly wider ($\sigma_v = 5.55\,\mathrm{mm\,yr^{-1}}$, $\mathrm{P05} = -12.3\,\mathrm{mm\,yr^{-1}}$, $\mathrm{P95} = +5.4\,\mathrm{mm\,yr^{-1}}$), spanning both subsiding and uplifting signals. This reflects the geomorphological diversity of the zone, which encompasses slow valley-floor subsidence, active slope deformation on Apennine and peri-Alpine hillsides, and localised deep-seated deformation signals, partly linked to debuttressing. The *accel* and *decel* classes are roughly balanced (1.1% vs. 1.2%), suggesting a population of slopes in different phases of kinematic activity, from reactivating landslides to seasonally modulated creep. Notably, the `jumpy` flag rate in this zone (71.8%) is the highest of the three, reflecting both phase unwrapping difficulties over high-relief terrain and genuine abrupt displacement events on steep slopes.

High-mountain zone ($>1500\,\mathrm{m}$ a.s.l.; 29,154,278 points, 10.3% of total). The high-mountain zone shows the most extreme classification pattern, with 83.9% of points assigned to the *noisy–stable* class — the highest fraction of any zone — and only 3.9% *stable*. This reflects the severe InSAR conditions above the snow line: rocky terrain with few artificial reflectors, persistent winter snow cover causing temporal decorrelation, and strong atmospheric phase screen residuals from orographic precipitation and vertical tropospheric gradients (Zebker et al., 1997). Critically, the *noisy* class in this zone has a near-zero mean velocity ($\bar{v} = +0.24\,\mathrm{mm\,yr^{-1}}$) with a symmetric, narrow range ($\mathrm{P05} = -1.3$, $\mathrm{P95} = +1.7\,\mathrm{mm\,yr^{-1}}$), in marked contrast to the systematic negative bias observed in both lower zones. This confirms that the high-mountain *noisy–stable* points are dominated by measurement noise rather than real deformation signals. The *linear* class (1.8%) shows the widest velocity spread of any class–zone combination ($\sigma_v = 9.66\,\mathrm{mm\,yr^{-1}}$; $\mathrm{P05} = -21.3$, $\mathrm{P95} = +6.2\,\mathrm{mm\,yr^{-1}}$), reflecting a heterogeneous population that includes fast-moving rockslide and DSGSD complexes, glacially influenced subsidence, periglacial frost-heave signals, and debuttressing. The `periodic` flag drops sharply from 25.5% in the plain zone to 10.9% in the high-mountain zone, consistent with the reduced contribution of infrastructure thermal deformation and groundwater-driven seasonal signals at high elevation.

5 Discussion

5.1 Geoscientific interpretation of deformation patterns

The classification of 282 M EGMS L2b coherent scatterers across northern Italy reveals a spatially organised pattern of ground deformation styles that is consistent with the regional geology and known geohazard inventory, providing a first-order validation of the EGMSpy classification scheme.

Systematic negative velocity bias and Po Plain consolidation. The most pervasive result is the negative velocity bias of the entire dataset ($\bar{v} = -0.93\,\mathrm{mm\,yr^{-1}}$) and the 3.2× longer negative tail of the velocity distribution ($\mathrm{P05} = -3.5$ vs $\mathrm{P95} = +1.1\,\mathrm{mm\,yr^{-1}}$). This asymmetry is a well-established physical signal of widespread, low-rate subsidence across the study area, driven by the compaction of Quaternary alluvial sediments under the combined influence of natural consolidation, groundwater extraction, and hydrocarbon production (Colesanti et al., 2003; Teatini et al., 2005; Cenni et al., 2021). The spatial gradient — from near-zero mean velocity in the high-mountain zone through the mid-mountain transition to the plain and low-hill zone (systematic $\approx -0.8\,\mathrm{mm\,yr^{-1}}$ even in nominally stable scatterers) — is captured by the elevation-zone analysis without any a priori spatial constraint.

The dominance of the *linear* class in the plain and low-hill zone (6.5% of zone points, vs. 3.3% mid-mountain and 1.8% high-mountain) and its strongly negative velocity distribution ($\bar{v} = -4.81\,\mathrm{mm\,yr^{-1}}$, with the entire 90th-percentile range remaining negative) are in close agreement with dedicated InSAR time series analyses of the same area. Chen et al. (2026) analysed EGMS Sentinel-1 data over the Po River Delta (a sub-region of our Po Plain zone) using a regression-based decomposition approach and found that the temporal behaviour of most PS points is *trend-dominated* — the equivalent of our *linear* class — with subsidence rates consistent with ongoing Holocene sediment compaction. Their spatial modelling of subsidence as a function of Holocene deposit age fitted a logarithmic relationship ($R^2 = 0.72$), confirming that natural consolidation is the dominant first-order control on Po Plain subsidence rates, with deviations from the modelled curve attributable to localised anthropogenic drivers such as groundwater extraction and infrastructure loading. Our median velocity for plain-zone *linear*-class points ($-4.1\,\mathrm{mm\,yr^{-1}}$) falls within the range predicted by Chen et al. (2026) logarithmic model for sediments of intermediate Holocene age (≈1,000–3,000 yr BP), and our P05 ($-10.6\,\mathrm{mm\,yr^{-1}}$) corresponds to rates expected from the most recent deltaic deposits (< 500 yr BP), where compressibility and consolidation rates are highest.

Accelerating and decelerating deformation. The slight excess of *accel* over *decel* points across the dataset (1.6% vs. 1.3%; ratio 1.23:1) is consistent with an ongoing but non-equilibrium consolidation process: subsidence is still predominantly accelerating rather than decelerating throughout most of the Po Plain, suggesting that the perturbations driving enhanced consolidation (groundwater abstractions, land reclamation, infrastructure loading) continue to outpace natural relaxation. In the plain and low-hill zone specifically, the mean velocity of the *accel* class ($-2.90\,\mathrm{mm\,yr^{-1}}$) confirms that accelerating deformation is predominantly confined to the subsidence domain. Chen et al. (2026) similarly found that abrupt changes detected by the BEAST algorithm along Po Delta levees are most often consistent with accelerated consolidation under structural loading, particularly where new road surfaces and built infrastructure have been added to unconsolidated deltaic deposits.

Seasonal signals: infrastructure vs. natural terrain. The `periodic` flag assigned to 23.7% of all points documents the pervasiveness of annual and semi-annual harmonic components in the displacement time series across the study area. However, the physical origin of this signal varies substantially by scatterer type. Chen et al. (2026) provide a key disambiguation: in the Po Delta, seasonal displacement signals are strongly concentrated on metal infrastructure — bridges and transmission towers — whose apparent deformation reflects thermal expansion and contraction of structural elements rather than true ground motion. Their analysis shows that bridge end-points can exhibit opposing correlations with land surface temperature (one end positive, the other negative), attributed to the differential thermal response along the bridge span. In natural terrain, the seasonal signal is primarily driven by pore pressure fluctuations associated with groundwater recharge cycles and, in peri-Alpine and Alpine areas, by local hydrological oscillations, freeze-thaw cycles, and snow loading effects. This distinction implies that a fraction of the 23.7% `periodic` points in our dataset are infrastructure scatterers responding to thermal forcing rather than recording hydrogeological or geotechnical ground motion. Separating these two populations — for example, by cross-referencing the `periodic` flag with land-use or infrastructure datasets — could be an useful future development to improve the geomorphological interpretability of the seasonal signal.

High-mountain zone: noise dominance and high-velocity outliers. The high-mountain zone's 83.9% *noisy–stable* fraction, near-zero mean velocity ($+0.24\,\mathrm{mm\,yr^{-1}}$), and symmetric velocity distribution confirm that this zone is dominated by measurement noise rather than geophysical signal, consistent with the severe InSAR conditions above the permanent snow line (Zebker et al., 1997). However, the *linear* class in the high-mountain zone shows the highest velocity standard deviation of any class–zone combination ($\sigma_v = 9.66\,\mathrm{mm\,yr^{-1}}$) and the widest P05–P95 range (-21.3 to $+6.2\,\mathrm{mm\,yr^{-1}}$), indicating a heterogeneous population of scattered, low-autocorrelation clusters that include both slow-moving landslides and deep-seated gravitational slope deformation (DSGSD) complexes alongside glacially-influenced motion. This heterogeneity in the *linear* class is consistent with the findings of Dong et al. (2025), who used a multimodal deep learning approach to classify EGMS-derived active deformation areas (ADAs) across Italy into four geophysical process types (landslide, subsidence, DSGSD, mining). Their classification of 99,402 Italian ADAs — identifying 71,101 landslides, 18,853 subsidence areas, 5,191 mining sites, and 4,257 DSGSDs — showed that mountainous regions with steep slopes and high elevations (as in our Alpine zone) are predominantly associated with landslide and DSGSD processes. Their explainable AI analysis further revealed that the two processes are the most commonly confused pair, with 84 misclassification cases on the ascending dataset, consistent with the inherent geomorphological similarity between deep-seated and shallow slope deformation at the millimetre-per-year displacement rates captured by EGMS.

5.2 Complementarity with existing classification frameworks

Time series pattern classification vs. process classification. EGMSpy's classification scheme assigns *time series behaviour labels* (stable, noisy–stable, linear, accel, decel, variable) to individual PS points. This is distinct from, and complementary to, the *geophysical process classification* approach of Dong et al. (2025), who assign process labels (landslide, subsidence, DSGSD, mining) to spatially coherent deformation clusters (ADAs) with supervised classification. The two approaches operate at different scales and use different information: EGMSpy uses per-point kinematic features extracted from the displacement time series alone, while the approach of Dong et al. (2025) additionally leverages DEM, slope, aspect, and optical imagery to capture the morphological context of each deforming area. Their ablation study demonstrates that TS information alone achieves only ≈61% mean F1 on the ascending dataset, while spatial and morphological features alone reach ≈81%, with the multimodal fusion achieving >91% overall accuracy. This result motivates a natural extension of EGMSpy: the cluster polygons produced by the velocity-weighted 3D DBSCAN step are direct analogues of ADAs, and could serve as the spatial units for a subsequent process-level classification step that incorporates DEM and land-cover variables. Such an integration would enable a seamless two-stage pipeline from raw EGMS data to geophysical process labels: EGMSpy handles the data management, time series characterisation, and clustering stages, while a process classifier such as that of Dong et al. (2025) would operate on the resulting cluster geometries.

Anomaly detection and critical infrastructure monitoring. The `jumpy` descriptor flag identifies points with abrupt displacement steps in their time series, a population that includes both genuine geophysical change points (e.g. triggered accelerations, levee deformation events) and measurement artefacts (phase unwrapping errors, processing discontinuities). Chen et al. (2026) demonstrate that the BEAST Bayesian change-point algorithm can reliably separate real from artefactual breaks in Po Delta PS time series, with posterior probabilities > 0.9 providing a conservative criterion for true structural change. In their study, BEAST-detected change points cluster spatially along levees, embankments, and urbanised areas, while geologically quiet zones show few significant breaks. This spatial pattern is directly consistent with the expected distribution of the `jumpy` flag in our dataset: if the flag were re-examined at a spatial scale (i.e., what fraction of flagged points lie along known infrastructure vs. natural terrain), the infrastructure-associated fraction would likely dominate. The high overall `jumpy` rate (63.3%) we observe across the full northern Italy dataset warrants careful interpretation, as noted in Section 4.2: a large fraction reflects noise in the *noisy–stable* class rather than true step events. Future work will apply probabilistic change-point detection analogous to Chen et al. (2026) to filter the `jumpy` population and identify the subset of infrastructure-associated change points with genuine monitoring significance.

5.3 Comparison with existing tools

It is useful to compare EGMSpy processing algorithms with those of existing available tools of similar scope and range. Table 9 summarises the capabilities of EGMSpy relative to tools commonly used for InSAR time series analysis and EGMS data access. The approaches of Chen et al. (2026) and Dong et al. (2025) are included for context, as they operate on the same EGMS data source.

Table 9: Capability comparison with related tools and approaches operating on Copernicus EGMS data. TS = time series; ADA = active deformation area.

Tool / Study	**Scope**	$N > 10^7$	**Key characteristic**
EGMS Explorer portal	Single-tile viewer	No	No classification, no multi-tile query
EGMStoolkit (Hrysiewicz et al., 2024)	Download utility	No	Download only; no analysis
Chen et al. (2026)	Regional (Po Delta)	Partial	TS pattern classification + BEAST anomaly detection; spatial subsidence modelling by deposit age
Dong et al. (2025)	National (Italy)	No	Process classification (landslide/subsidence/DSGSD/mining) via multimodal CNN–LSTM fusion on ADAs
MintPy (Yunjun et al., 2019)	Upstream processing	Partial	Raw SLC → TS; not applicable to EGMS product
EGMSpy (this work)	Regional to continental	Yes	End-to-end data handling, per-point TS classification, 3D DBSCAN clustering, interactive web viewer; complements Chen et al. 2026 and Dong et al. 2025

5.4 Scalability and hardware requirements

The current implementation processes the 282 M-point northern Italy dataset on a single workstation (AMD Threadripper 3970X, 274 GB RAM) without distributed computing. The dominant bottleneck is time series classification (≈24–48 h for 434 tiles at 32 joblib workers), which is tile-parallel. DuckDB viewport queries over the full in-memory database complete in 30–80 ms regardless of dataset size, providing a smooth visualisation and management for users.

Scaling to the full EGMS dataset (≈5 B points, ∼10,000 tiles) will require migration to GPU-accelerated DBSCAN and GMM (RAPIDS cuML) on a multi-GPU server, with DuckDB Parquet predicate pushdown via a sidecar spatial bounding-box index for tile skipping. The split-GeoParquet tile-per-file architecture is designed to support this transition without any schema changes. However, this kind of application is beyond the scope of the present paper.

A critical performance note: NumPy must be MKL-linked (not OpenBLAS) on AMD platforms. The OpenBLAS default in the `conda-forge` channel produces a ≈40× slowdown in the feature extraction batch OLS on the Threadripper workstation.

5.5 Limitations and possible developments

Absolute vs. relative jump thresholds. Jump and noise detection thresholds are currently fixed at 5 mm. Fast-moving points ($|v| > 30\,\mathrm{mm\,yr^{-1}}$) may have intrinsically larger first differences, causing under-detection of real geophysical jumps. A relative threshold normalised by local velocity magnitude is planned in the next releases. In the meantime, interested users are encouraged to try out different thresholds to experiment model sensitivity.

Winter gap correction. Acquisition gaps (predominantly November–March in Alpine regions) are filled with linear interpolation. A model-driven approach based on regional groundwater or snow-depth climatology would be more physically consistent and could reduce the *noisy–stable* fraction in Alpine areas. We have also experimented different parameters for gap detection and correction in longer-winter regions, such as Iceland, with notable improvements in the model capability to correctly classify winter gap-affected TS.

Probabilistic change-point detection. In the next releases of EGMSpy, we plan to supplement the binary `jumpy` flag with probabilistic change-point estimates, following the Bayesian approach demonstrated by Chen et al. (2026) for the Po Delta. This will enable infrastructure monitoring applications analogous to their levee-surveillance framework.

Process-level classification. The cluster polygons produced by EGMSpy's 3D DBSCAN provide a natural input for a subsequent process-level classification stage. Integration with the multimodal CNN–LSTM framework of Dong et al. (2025), or similar approaches, which incorporate DEM, slope, and optical imagery, is planned to enable end-to-end labelling from raw EGMS tiles to geophysical process types (landslide, subsidence, DSGSD, mining, or more detailed categories).

Cross-orbit integration. Ascending and descending LOS velocities are currently processed independently. Fusion into vertical and east–west displacement components (Bovenga et al., 2012; Farolfi et al., 2019) is planned for the next release.

Validation. A rigorous validation of the time series classification against the Italian Landslide Inventory (PAI/IFFI), ground-truth InSAR surveys, and GNSS time series will be reported in the companion application paper.

AI assistance declaration: AI-assisted writing tools were used for copy editing of this manuscript, comprising improvements to readability, style, grammar, and formatting, in accordance with Springer Nature editorial policy. All scientific content, data analysis, results, and interpretations are the sole work and responsibility of the human authors.

6 Conclusions

We have presented MISSlab EGMS InSAR Tools, an open-source Python pipeline for end-to-end processing, classification, clustering and interactive visualisation of Copernicus EGMS L2b ground motion data at regional scale. The key innovations are: (i) a split-GeoParquet/DuckDB storage architecture that enables sub-100 ms analytical queries over hundreds of millions of points on commodity hardware; (ii) a physics-informed hybrid rule/GMM time series classifier that assigns geophysically interpretable labels to every InSAR point without requiring manual parameter tuning; (iii) a velocity-weighted 3D DBSCAN clustering algorithm that identifies spatially and dynamically coherent deformation areas; and (iv) a canvas-based interactive web viewer capable of rendering 200,000+ classified points in a single draw call.

Internal quality control on a random sample of 99,751 northern Italy measurement points confirms that the toolkit's OLS feature extraction is consistent with the official EGMS pre-computed velocities to within 0.096 mm yr^{-1} RMSE — one order of magnitude below the EGMS measurement precision — with no systematic bias across the full velocity range.

Full quantitative results for the northern Italy dataset (≈300 M points) and geoscientific interpretation will be presented in the companion application paper (in preparation, *Computers & Geosciences*).

6 Availability and Requirements

- **Project name:** EGMSpy
- **Project home page:** https://github.com/MISSLab-Padova/egmspy (in preparation)
- **Operating system(s):** Windows 10/11, Linux (Ubuntu 22.04)
- **Programming language:** Python 3.12
- **Required packages:** `pandas`, `geopandas`, `pyarrow`, `duckdb`, `scikit-learn`, `scipy`, `shapely`, `tqdm`, `pyqt6`, `flask`, `flask-cors`, `fiona`, `gdal`, `joblib` (all via `conda-forge`); `plotly`, `kaleido`, `concave-hull` (via `pip`)
- **Minimum hardware:** 8 GB RAM, multi-core CPU. For >50 M points: ≥64 GB RAM recommended. Production runs (>200 M points): ≥128 GB RAM, 32+ cores
- **Licence:** MIT
- **Any restrictions to use by non-academics:** None

6 Data and code availability

EGMS L2b data are freely available from the Copernicus Land Monitoring Service (https://egms.land.copernicus.eu/) subject to the Copernicus Data Policy. The MISSlab EGMS InSAR Tools source code will be released under the MIT licence at https://github.com/MISSLab-Padova/egms-insar-tools (repository in preparation; available upon acceptance).

6 Statements and Declarations

Funding. This work was supported by the RETURN Extended Partnership and received funding from the European Union Next-GenerationEU (National Recovery and

Resilience Plan — NRRP, Mission 4, Component 2, Investment 1.3 — D.D. 1243 2/8/2022, PE0000005).

Competing interests. The authors declare no competing interests.

Author contributions. F.C.: conceptualisation, methodology, software development, data curation, formal analysis, writing — original draft, review and editing.

A Pipeline performance benchmarks

Table 10: Observed and estimated runtimes for the northern Italy dataset (434 tile pairs, ≈300 M points) on the AMD Threadripper 3970X workstation (274 GB RAM, MKL-linked NumPy, Windows High Performance power plan).

Step	Runtime	Notes
Download (517 tiles, ≈180 GB)	∼3 h	Network-limited
CSV to GeoParquet (434 tiles)	∼8–12 h	I/O-limited
Tile index (434 tiles)	∼5 min	16 workers, 1.55 files s^{-1}
TS classification	∼24–48 h	32 joblib workers
DBSCAN clustering	∼15–30 min	`n_jobs=-1`, ball tree
Sub-clustering	∼2–4 h	32 workers, generator dispatch
Parquet write-back	∼10–20 min	16 parallel writers
DuckDB viewport query (300 M pts)	30–80 ms	In-memory, CTE plan

B Installation and environment

```
conda create -n egms_tool python=3.12
conda activate egms_tool
conda install -c conda-forge pandas geopandas pyarrow duckdb \
    scikit-learn scipy shapely tqdm pyqt6 flask flask-cors \
    fiona gdal joblib
pip install alive-progress plotly kaleido concave-hull

# MKL-linked NumPy -- required on workstation for correct performance
conda install -c anaconda mkl numpy scikit-learn --force-reinstall

# EGMStoolkit (download step only)
git clone https://github.com/alexisInSAR/EGMStoolkit.git
echo PATH_TO/EGMStoolkit/src > \
    $CONDA_PREFIX/Lib/site-packages/egmstoolkit.pth
```

Windows only (if `ImportError: _ctypes`):

```
copy ffi.dll %CONDA_PREFIX%\DLLs\ffi.dll
copy ffi.dll %CONDA_PREFIX%\DLLs\libffi-8.dll
```

B References

P. Berardino, G. Fornaro, R. Lanari, and E. Sansosti. A new algorithm for surface deformation monitoring based on small baseline differential SAR interferograms. *IEEE Transactions on Geoscience and Remote Sensing*, 40(11):2375–2383, 2002. doi:10.1109/TGRS.2002.803792.

M. Berti, A. Corsini, S. Franceschini, and J. P. Iannacone. Automated classification of persistent scatterers interferometry time series. *Natural Hazards and Earth System Sciences*, 13(8):1945–1958, 2013. doi:10.5194/nhess-13-1945-2013.

F. Bovenga, J. Wasowski, D. Nitti, R. Nutricato, and M. Chiaradia. Using COSMO/SkyMed X-band and ENVISAT C-band SAR interferometry for landslides analysis. *Remote Sensing of Environment*, 119:272–285, 2012. doi:10.1016/j.rse.2011.12.013.

N. Casagli, E. Intrieri, V. Tofani, G. Gigli, and F. Raspini. Landslide detection, monitoring and prediction with remote-sensing techniques. *Nature Reviews Earth & Environment*, 4(1):51–64, 2023. doi:10.1038/s43017-022-00373-x.

N. Cenni, S. Fiaschi, and M. Fabris. Monitoring of land subsidence in the Po Plain (Northern Italy) using GNSS and InSAR data. *Geomatics, Natural Hazards and Risk*, 12(1):2960–2987, 2021. doi:10.1080/19475705.2021.1986317.

X. Chen, P. Teatini, A. Rosi, F. Catani, and M. Floris. Spatiotemporal dynamics and anomaly detection of land subsidence in delta areas: A case study from the Po river delta using InSAR time series. *IEEE Journal of Selected Topics in Applied Earth Observations and Remote Sensing*, 19:10381–10393, 2026. doi:10.1109/JSTARS.2025.3650597.

F. Cigna, C. Del Ventisette, V. Liguori, and N. Casagli. Advanced radar-interpretation of InSAR time series for mapping and characterisation of geological processes. *Natural Hazards and Earth System Sciences*, 11(3):865–881, 2011. doi:10.5194/nhess-11-865-2011.

C. Colesanti, A. Ferretti, F. Novali, C. Prati, and F. Rocca. SAR monitoring of progressive and seasonal ground deformation using the permanent scatterers technique. *IEEE Transactions on Geoscience and Remote Sensing*, 41(7):1685–1701, 2003. doi:10.1109/TGRS.2003.813518.

M. Costantini, A. Ferretti, F. Minati, S. Falco, F. Trillo, D. Colombo, F. Novali, F. Malvarosa, C. Mammone, F. Vecchioli, A. Rucci, A. Fumagalli, J. Allievi, M. G. Ciminelli, and S. Costabile. Analysis of surface deformations over the whole Italian territory by interferometric processing of ERS, Envisat and COSMO-SkyMed radar data. *Remote Sensing of Environment*, 202:250–275, 2017. doi:10.1016/j.rse.2017.07.017.

M. Crosetto, L. Solari, M. Mróz, J. Balasis-Levinsen, N. Casagli, M. Frei, A. Oyen, D. Moldestad, L. Bateson, L. Guerrieri, V. Comerci, and H. Andersen. The evolution of wide-area DInSAR: From regional and national services to the European Ground Motion Service. *Remote Sensing*, 12(12):2043, 2020. doi:10.3390/rs12122043.

Y. Dong, L. Nava, R. Palamà, O. Monserrat, D. Festa, M. Floris, A. Rosi, and F. Catani. Improving ground deformation classification by integrating InSAR time series with geospatial information. *IEEE Transactions on Geoscience and Remote Sensing*, 63: 4709412, 2025. doi:10.1109/TGRS.2025.3635271.

M. Ester, H.-P. Kriegel, J. Sander, and X. Xu. A density-based algorithm for discovering clusters in large spatial databases with noise. In *Proceedings of the Second International Conference on Knowledge Discovery and Data Mining (KDD-96)*, pages 226–231. AAAI Press, 1996.

G. Farolfi, A. Piombino, and F. Catani. Fusion of GNSS and satellite radar interferometry: Determination of 3D fine-scale map of present-day surface displacements in Italy as expressions of geodynamic processes. *Remote Sensing*, 11(4):394, 2019. doi:10.3390/rs11040394.

A. Ferretti, C. Prati, and F. Rocca. Permanent scatterers in SAR interferometry. *IEEE Transactions on Geoscience and Remote Sensing*, 39(1):8–20, 2001. doi:10.1109/36.898661.

P. Fredi and E. Lupia Palmieri. *Il paesaggio fisico della Terra*. Zanichelli, Bologna, 2004.

E. Ghaderpour, P. Mazzanti, F. Bozzano, and G. S. Mugnozza. A fast and robust method for detecting trend turning points in InSAR displacement time series. *Computers & Geosciences*, 185:105546, 2024. doi:10.1016/j.cageo.2024.105546.

A. Hooper. A multi-temporal InSAR method incorporating both persistent scatterer and small baseline approaches. *Geophysical Research Letters*, 35(16):L16302, 2008. doi:10.1029/2008GL034654.

A. Hooper, D. Bekaert, K. Spaans, and M. Arıkan. Recent advances in SAR interferometry time series analysis for measuring crustal deformation. *Tectonophysics*, 514–517:1–13, 2012. doi:10.1016/j.tecto.2011.10.013.

A. Hrysiewicz, K. Spaans, and A. Hooper. EGMStoolkit: a Python toolkit for downloading and processing European Ground Motion Service (EGMS) data. *Earth Science Informatics*, 17:3117–3126, 2024. doi:10.1007/s12145-024-01356-w.

S. M. Mirmazloumi, Y. Wassie, J. A. Navarro, R. Palamà, V. Krishnakumar, A. Barra, M. Crosetto, and O. Monserrat. Classification of ground deformation using Sentinel-1 persistent scatterer interferometry time series. *GIScience & Remote Sensing*, 59(1): 374–392, 2022. doi:10.1080/15481603.2022.2030535.

F. Raspini, S. Bianchini, A. Ciampalini, M. Del Soldato, R. Montalti, L. Solari, V. Tofani, and N. Casagli. Continuous, semi-automatic monitoring of ground deformation using Sentinel-1 satellites. *Scientific Reports*, 9:7253, 2019. doi:10.1038/s41598-019-43884-8.

P. Teatini, L. Tosi, T. Strozzi, L. Carbognin, U. Wegmüller, and F. Rizzetto. Mapping regional land displacements in the Venice coastland by an integrated monitoring system. *Remote Sensing of Environment*, 98:403–413, 2005. doi:10.1016/j.rse.2005.08.002.

C. Werner, U. Wegmüller, T. Strozzi, and A. Wiesmann. GAMMA SAR and interferometric processing software. In *Proceedings of the ERS–Envisat Symposium*, Gothenburg, Sweden, 2000. ESA SP-461.

Z. Yunjun, H. Fattahi, and F. Amelung. Small baseline InSAR time series analysis: unwrapping error correction and noise reduction. *Computers & Geosciences*, 133:104331, 2019. doi:10.1016/j.cageo.2019.104331.

H. A. Zebker, P. A. Rosen, and S. Hensley. Atmospheric effects in interferometric synthetic aperture radar surface deformation and topographic maps. *Journal of Geophysical Research: Solid Earth*, 102(B4):7547–7563, 1997. doi:10.1029/96JB03804.